KRONOS FUSION ENERGY

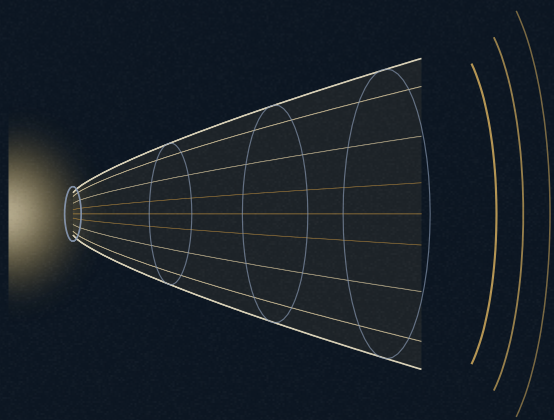

PAPER 2.56 · THE KRONOS 2026 SERIES

ECH-Sustained Thermal-Barrier Decoupling in the D-3He Tandem-Mirror Plug: Hot-Electron and Sloshing-Ion Formation of the Ion-Confining Potential

The recirculating power of a tandem-mirror fusion burner is set almost entirely by the electrostatic potential the end plugs must raise to confine the central-cell ions, and in a...

Read it live — 3-D model · physics validator · film series

BY P I FORD AND G L KULCINSKI

2026 · EDITORIAL EDITION

THE OFFICIAL RECORD

What this document is, and how to read its numbers

This is a combined editorial. It gathers, in one volume, the two design studies Kronos Fusion Energy released in 2026 — a compact spherical-tokamak tritium/helium-3 breeder and a deuterium–helium-3 tandem-mirror generator — together with the intellectual-property estate, the people, and, in the internal edition, the full commercial case. The scientific text is the same text that appears in the arXiv preprints and the journal submissions; the editorial adds the apparatus a reader needs to hold the whole program at once, and nothing in the physics is altered to fit it.

THE HONESTY STANCE IS THE ASSET

Every headline quantity carries an **evidence class** — DERIVED RECOMPUTED MEASURED REQUIREMENT — and, where a number is a modelled extrapolation rather than a demonstrated value, it is labelled as such and its downside is shown next to it. Several quantities in the underlying corpus moved after first publication; where a value has been withdrawn or restated, the record says so plainly. This is deliberate: a diligence team will find the load-bearing assumptions, so the document surfaces them first.

TWO EDITIONS

This volume is issued in two editions. The **public edition** (light) carries the physics and the design only — no dollar, price, or per-kilogram figure appears anywhere in it. The **internal edition** (dark) adds the economics, the funding architecture, and the defense-commercial analysis, and is marked *Confidential* accordingly; it is not for public distribution. Where the commercial case rests on a modelled assumption rather than a demonstrated one, it is labelled as such and its downside is shown alongside it, on the same terms as the physics.

TITLE	The Kronos Fleet — Hyperion · Aegis · MetroVolt: A Combined Design & Commercialization Study
AUTHOR	Priyanca Ford, Founder & CEO, on behalf of Kronos Fusion Energy
EDITION	2026 Combined Editorial · first issue
COMPANION WORKS	The five-paper arXiv drop — (1) Breeder, (2) Burner, (3) REBCO magnet & tape, (4) Direct Energy Conversion, (5) AI/ML/Quantum control — with matching numbered Zenodo deposits, plus the IOP journal and IAEA-FEC submissions. Patents were filed before the drop.
NAMING	Hyperion = the breeder; Aegis (defense) and MetroVolt (data-center) = one generator in two housings. Internal mode letters (D1, L) do not appear on public surfaces.
STATUS	Conceptual design & simulation study. Nothing herein is a construction commitment.

HOW TO READ THIS VOLUME

The fleet at a glance, and the way its numbers are marked

This volume opens with *Orientation*, presents the five research papers as a bound sequence, and closes with the *Apparatus*. *Foundations* sets out the three general results both machines rest on. *Paper One* is the Hyperion breeder; *Paper Two* the Aegis / MetroVolt generator; *Papers Three, Four and Five* are the enabling science — high-field REBCO magnets and tape, direct energy conversion, and the AI / ML / quantum control stack. A *Digital Twin & 3-D Model* part follows, then the *Environmental* profile. The *Economics* and levelized cost and the *Business Case* and diligence record appear in the internal edition only; the *Simulations* proof record and the Apparatus — patent portfolio, team, limitations, and sources — close both editions.

THE FLEET AT A GLANCE

	HYPERION	AEGIS	METROVOLT
Role	Strategic-isotope foundry	Defense installation power	Campus power
Machine	**Spherical tokamak**	**Tandem mirror**	**Tandem mirror**
Fuel	Deuterium–tritium	Deuterium–helium-3	Deuterium–helium-3
Delivers	Tritium · ^{3}He · 14 MeV n	Resilient installation power	Firm campus power
Physics bar	**Fusion gain only**	Closure (gates named)	Closure + lunar ^{3}He
In the fleet	Breeds the fuel	Proves the generator	Commercial destination

HOW THE NUMBERS ARE MARKED

Every headline quantity carries an evidence class — DERIVED from first principles, RECOMPUTED from raw data, MEASURED in hardware, or a REQUIREMENT yet to be met. Financial figures carry a case label and are confined to the internal (confidential) edition. Values that moved after first publication are shown as withdrawn or restated rather than quietly changed. A capability you can evaluate is one whose limits are on the page.

ABSTRACT

ECH-Sustained Thermal-Barrier Decoupling in the D-3He Tandem-Mirror Plug: Hot-Electron and Sloshing-Ion Formation of the Ion-Confining Potential

The recirculating power of a tandem-mirror fusion burner is set almost entirely by the electrostatic potential the end plugs must raise to confine the central-cell ions, and in a deuterium–helium-3 (D–^{3}He) machine that potential is large: the frozen Kronos burner design point demands an ion-confining potential $\phi_i \simeq 248.75\,\mathrm{keV}$ at an ion temperature $T_i \simeq 90\,\mathrm{keV}$ ($e\phi_i/T_i = 2.764$), a mirror ratio $R_{\mathrm{mc}} = 4.61$, and an engineering gain $Q_E = 1.318$ that sits only just above break-even. The binding constraint is that, when the plug electrons and the central-cell electrons are Boltzmann-connected along the field line, raising ϕ_i requires raising the central-cell electron temperature, and heating the whole central column to hold the potential costs a frozen $1092.5\,\mathrm{MW}$ of electron-cyclotron power. We formalise the *thermal-barrier* mechanism that breaks this coupling. A localised depression of the electron density and potential, sustained jointly by electron-cyclotron-heated (ECH) hot electrons and a sloshing-ion population whose turning points bracket the barrier, thermally isolates the plug electrons from the central-cell electrons, so the confining potential is set by a hot *plug* electron temperature and a density ratio rather than by the central-cell temperature. We derive the field-line potential structure, the barrier-depth decoupling condition $e\phi_b/T_e \geq \ln(n_c/n_b)$, the sloshing-ion density profile from the adiabatic invariants, and the Pastukhov confinement scaling $n\tau_p \propto (e\phi_i/T_i)\,\mathrm{e}^{e\phi_i/T_i}$, and we solve the coupled quasineutrality–confinement–power balance self-consistently. Booking the barrier, the confining-potential requirement falls to $\phi_i \simeq 167.9\,\mathrm{keV}$ — a 33% cut in the binding gate, dominated by making T_i the lever — and the $1092.5\,\mathrm{MW}$ of central-cell heating is removed from the recirculating budget, lifting Q_E from 1.318 toward 3–5 in the fully realised limit. The kinetic barrier model (bounce-averaged Fokker–Planck) and the loss-cone microstability bound (warm-fill knee at 6.25%; residual Alfv\'en ion-cyclotron activity at $\gamma/\omega_{ci} \simeq 0.037$) are computed on the NVIDIA GPU high-performance-computing campaign. Against the TMX-U, GAMMA-10 and gas-dynamic-trap thermal-barrier records the mechanism is well precedented; its single retirement experiment is a WHAM-scale barrier demonstration. Every headline quantity is a frozen anchor (gate KX-L1-A13-BU) in the Kronos Physics De-Risking Register.

Open-access deposit (code & data, CC BY 4.0): DOI 10.5281/zenodo.22645781 · Zenodo community *kronos_fusion_energy*. Explore it live: interactive 3-D model · physics validator.

Keywords: tandem mirror · thermal barrier · sloshing ions · electron-cyclotron heating · Pastukhov confinement · plug potential · recirculating power · D--^{3}He

CONTENTS

Table of Contents

NOMENCLATURE

Symbols, units, and the names of things

Q	plasma (fusion) gain, P_{fus}/P_{aux}
Q_E	engineering gain, net electric out / recirculating in
H_{98}	confinement enhancement over the IPB98(y,2) scaling
Z_{eff}	effective ion charge
c_{ee}	electron–electron bremsstrahlung leading coefficient, 2.120022 (exact)
τ_E	energy confinement time
I_p	plasma current
R_0, a	major radius, minor radius
κ, δ	elongation, triangularity
β_N	normalized plasma beta (Troyon-normalized)
TBR	tritium breeding ratio
DEC	direct energy conversion
CF	plant capacity factor (availability)
FOAK / NOAK / BOAK	first / nth / best of a kind
Hyperion	the ST breeder (internal: Mode D2)
Aegis	the generator, defense/installation housing (internal: Mode M)
MetroVolt	the generator, data-center housing (Mode M)

§ 1

Introduction

THE TANDEM MIRROR AND THE COST OF THE PLUG

A tandem mirror confines a long, low-field central cell between two high-field end plugs that raise an electrostatic potential to reflect the central-cell ions [6,7,8]. Unlike a closed toroidal device, an open mirror has no rotational transform and therefore no bootstrap current, no disruptions and no requirement for a divertor of the tokamak kind; the price for that simplicity is that the ion end-loss is governed directly by an electrostatic barrier, and the power needed to maintain that barrier is the machine's dominant recirculating load. In a deuterium–helium-3 (D–^{3}He) burner the price is steep, because the optimum ion temperature is high — of order $90\,\mathrm{keV}$ — and the confining potential must scale with it. The Kronos burner closes its zero-dimensional power balance at a design point (gate BU-L1-A1) with fusion power $P_{\mathrm{fus}} = 4298.5\,\mathrm{MW}$, neutron power $P_n = 233.95\,\mathrm{MW}$ (neutron fraction $f_n = 5.44\%$), engineering gain $Q_E = 1.318$, and an ion-confining potential $\phi_i = 248.75\,\mathrm{keV}$ [28,29]. The gain sits only 32% above engineering break-even; the plug is the binding gate.

WHY THE POTENTIAL IS EXPENSIVE: THE BOLTZMANN COUPLING

The reason the plug is expensive is a coupling, not a magnet limit. Along a magnetic field line the electrons of each connected population sit in Boltzmann equilibrium with the potential, so their density is tied to the local potential through their temperature. If the plug electrons and the central-cell electrons are one connected population, then the potential difference the plug can sustain is fixed by the central-cell electron temperature and a density ratio. To raise the confining potential one must then raise the central-cell electron temperature, and heating the entire central column with electron-cyclotron waves to hold that temperature is what costs the frozen $1092.5\,\mathrm{MW}$ [28]. The machine is dragged upward by its own electrons.

THE THERMAL BARRIER

Baldwin and Logan [5] recognised that this coupling can be broken by inserting, between the central cell and the plug, a local depression of the electron density and potential — a *thermal barrier* — that thermally isolates the two electron populations. Once decoupled, the plug electrons can be heated to a high temperature independently, and the confining potential is set by the *plug* electron temperature and a local density ratio; the central-cell electrons stay cool. The barrier is not free: it must be dug and held against collisional filling. In practice it is sustained by two ingredients acting together: ECH-driven mirror-trapped hot electrons, whose diamagnetic pressure deepens the magnetic and electrostatic well, and a *sloshing-ion* population — ions injected at a pitch angle so their turning points sit on either side of the barrier midplane, producing a density minimum at the midplane. The concept was demonstrated on the tandem mirror experiments TMX-U [11] and, with distinction, on GAMMA-10, where an energetic-electron-confining potential and transport barrier were formed and controlled [12]; the gas-dynamic trap has since shown that modern ECH can raise mirror electron temperatures far beyond the classical expectation [13,14], and the Wisconsin HTS Axisymmetric Mirror (WHAM) provides a high-field, high-density platform on which a barrier can be dug and diagnosed at reactor-relevant parameters [15].

CONTRIBUTION

This paper does three things. First (section 2) it states the thermal-barrier decoupling as a formal boundary-value problem on the field line: the Boltzmann relations for the connected and decoupled electron populations, the barrier-depth condition, the sloshing-ion density profile from the adiabatic invariants, the hot-electron diamagnetic well, and the Pastukhov ion-confinement scaling, closed against the self-consistent ambipolar potential and the burner power balance. Second (section 3) it describes the NVIDIA GPU high-performance-computing (HPC) campaign that produced the anchored numbers — the reduced-order mirror engine that closes the zero-dimensional balance, the bounce-averaged Fokker–Planck solve of the sloshing distribution and ambipolar potential, and the particle-in-cell and kinetic-dispersion evaluation of the loss-cone microstability bound — with its verification and reproducibility. Third (sections 4 –5) it reports the result: the confining-potential requirement drops from $248.75\,\mathrm{keV}$ to $167.9\,\mathrm{keV}$ (a 33% cut), the $1092.5\,\mathrm{MW}$ of central-cell ECH is removed, Q_E lifts from 1.318 toward 3–5, and the whole reduction is retired by a single WHAM-scale experiment. Every quantitative claim is a frozen anchor in the de-risking register [28]; the aggressive Q_E range is explicitly a model-limit and is flagged as such (section 6).

§ 2

Governing equations and the formal problem

FIELD-LINE COORDINATES AND THE BOLTZMANN RELATION

We work along a single magnetic field line parametrised by arc length z, with the field strength $B(z)$ forming a symmetric well between the central-cell midplane ($z = 0$, $B = B_{\min}$) and the mirror throat ($B = B_{\max}$), of mirror ratio $R_{\mathrm{mc}} \equiv B_{\max}/B_{\min} = 4.61$. The electrostatic potential $\phi(z)$ and the field are the unknowns of the equilibrium; particle motion conserves the magnetic moment $\mu = mv_\perp^2/2B$ and the total energy $\mathcal{E} = \frac{1}{2}m(v_\parallel^2 + v_\perp^2) + q\phi$.

Each electron population that is collisionally connected across a region sits, to leading order in the small electron mass, in Boltzmann equilibrium with the potential,

$$n_e(z) = n_{e0}\,\exp\!\left(\frac{e\,[\phi(z) - \phi_0]}{T_e}\right),$$

with n_{e0} and ϕ_0 reference values and T_e the temperature of that connected population. The ions, being nearly unmagnetised on the parallel scale, are described by their guiding-centre distribution and enter through quasineutrality,

$$\sum_s q_s\, n_s\big(\phi(z), B(z)\big) = 0,$$

summed over the fuel ions (D, ^{3}He), the fusion products, and the electron populations. Equations 1–2 determine $\phi(z)$ once the trapped-particle populations are specified. The confining potential seen by a central-cell ion is the height it must climb from the central-cell midplane to the potential peak in the plug,

$$\phi_i \equiv \phi_{\mathrm{peak}} - \phi(0).$$

THE BARRIER-LESS COUPLING AND THE RECIRCULATING-POWER PENALTY

Consider first the machine *without* a thermal barrier, so the plug electrons and the central-cell electrons form one connected population at temperature T_{ec}. Applying 1 between the central-cell midplane (density n_c) and the plug potential peak (density n_p) gives the confining potential directly,

$$\phi_i^{(\text{no barrier})} = \frac{T_{ec}}{e}\ln\frac{n_p}{n_c}.$$

The confining potential is chained to the central-cell electron temperature: a large ϕ_i demands a large T_{ec}. The central-cell electron power balance then carries the cost. Writing P_{ECH}^{cc} for the electron-cyclotron power delivered to the central column and τ_{Ee} for its electron energy-confinement time,

$$P_{\mathrm{ECH}}^{cc} \simeq \frac{3}{2}\,\frac{n_c T_{ec}\, V_c}{\tau_{Ee}} + P_{\mathrm{rad}}(T_{ec}),$$

with V_c the central-cell volume and P_{rad} the radiated (bremsstrahlung and synchrotron) power, which itself grows with T_{ec}. At the D–^{3}He operating point the required T_{ec} to sustain $\phi_i = 248.75\,\mathrm{keV}$ forces $P_{\mathrm{ECH}}^{cc} = 1092.5\,\mathrm{MW}$ [28]. This is the term the thermal barrier is designed to delete.

THERMAL-BARRIER DECOUPLING

Now insert a local minimum of the potential, the barrier, of depth ϕ_b below the central-cell potential, located between the central cell and the plug. The barrier interrupts the parallel electron flux: an electron of the central-cell population must, to reach the plug, first climb the barrier. The two electron populations decouple when the parallel flux over the barrier falls below the collisional supply from the central cell, which — inserting the Boltzmann factor for the flux suppression across a potential step of depth ϕ_b at temperature T_e — is the condition

$$\boxed{\frac{e\,\phi_b}{T_e} \;\geq\; \ln\frac{n_c}{n_b}}$$

where n_b is the density at the bottom of the barrier and n_c the central-cell density. Equation 6 is the decoupling criterion: once satisfied, the plug electrons behave as a separate population at their own (hot) temperature T_{eh}. The confining potential is then set on the *plug* side of the barrier,

$$\phi_i^{(\text{barrier})} = \phi_b + \frac{T_{eh}}{e}\ln\frac{n_p}{n_b},$$

in which T_{ec} no longer appears. The central cell may be held cool while the plug holds a large potential; the $1092.5\,\text{MW}$ of 5 is not spent. This is the entire lever of the paper, and equations 4 and 7 are its two poles.

SLOSHING-ION FORMATION OF THE BARRIER DENSITY MINIMUM

The barrier density minimum is dug in part by *sloshing ions*: energetic ions injected (by neutral beams or by the natural plug population) at the barrier midplane field B_0 with a pitch angle θ_0 chosen so their turning points lie between the midplane and the throat. From μ and $\mathcal{E}$ conservation, neglecting the potential over the beam energy, the pitch angle evolves along the field as

$$\sin^2\theta(B) = \frac{B}{B_0}\sin^2\theta_0,$$

so the ion mirrors (turns) where $\sin^2\theta = 1$, at the turning field

$$B_t = \frac{B_0}{\sin^2\theta_0}.$$

The parallel speed is $v_\parallel(B) = v_0\sqrt{1-(B/B_0)\sin^2\theta_0}$, and the density along a flux tube of cross-section $A(B)\propto 1/B$ follows from flux conservation of the guiding centres,

$$n_s(B) = \frac{\Gamma_s}{A(B)\,|v_\parallel(B)|} \;\propto\; \frac{B/B_0}{\sqrt{1-(B/B_0)\sin^2\theta_0}},$$

which is minimal at the midplane and rises to an integrable singularity at the turning points $B\to B_t$. A population injected so that its turning points straddle the barrier therefore piles up at the two turning points and is rarefied at the midplane, producing exactly the density minimum that 6 requires. The loss-cone half-angle for the burner mirror ratio,

$$\theta_{\text{lc}} = \arcsin\sqrt{\tfrac{1}{R_{\text{mc}}}} = 27.77^\circ,$$

sets the floor on the sloshing injection angle: the ions must be injected outside the loss cone ($\theta_0 > \theta_{\text{lc}}$) to be confined at all. Figure 4 plots 10 for the burner well.

HOT-ELECTRON DIAMAGNETIC WELL

The second barrier ingredient is a mirror-trapped hot-electron population produced by ECH at the electron cyclotron resonance. Their perpendicular pressure $p_{eh,\perp} = n_{eh}T_{eh}$ diamagnetically depresses the field in the resonant zone, deepening the magnetic well by $\delta B/B \simeq -\beta_{eh}/2$ with the hot-electron beta $\beta_{eh} = 2\mu_0 p_{eh,\perp}/B^2$; the deeper well in turn deepens the potential depression through 2. The trapped hot electrons contribute a Yushmanov potential [10] that holds warm ions in the barrier region and thereby regulates the barrier filling. In the reduced model the hot-electron population enters through an effective barrier temperature T_{eh} and a trapped fraction that sets n_b/n_c; both are inputs to the ambipolar solve of section 3 and are anchored to the kinetic Fokker–Planck result.

PASTUKHOV ION CONFINEMENT AND THE CONFINING-POTENTIAL REQUIREMENT

The central-cell ions are lost by pitch-angle scattering into the loss cone against the confining potential ϕ_i. Pastukhov's solution of the Fokker–Planck problem for an electrostatically-plugged mirror, refined by Cohen *et al* [1,2,3], gives the ion particle-confinement time as an exponential function of the normalised potential $u \equiv e\phi_i/T_i$,

$$n\,\tau_p \;=\; \frac{g(R_{\rm mc})}{\sqrt{\pi}}\;\frac{n\,\tau_{ii}}{\ln(2R_{\rm mc})}\;u\,{\rm e}^{\,u}, \qquad g(R_{\rm mc}) = \frac{2R_{\rm mc}+1}{2R_{\rm mc}}\,\ln(4R_{\rm mc}+2),$$

with τ_{ii} the ion–ion collision time. The exponential in 12 is why the potential is the binding gate: a modest change in u moves the confinement, and hence Q_E, by a large factor. At the burner design point $u = e\phi_i/T_i = 2.764$ (i.e. $\phi_i = 248.75\,\mathrm{keV}$, $T_i \simeq 90\,\mathrm{keV}$), and the plug ion-confinement time closes at $\tau_p = 3.73$ s [28]. The requirement, inverted, is that closing the machine at a given Q_E demands a minimum u, and any lever that raises T_i (which lowers the required u for a fixed absolute confinement, because $\tau_{ii} \propto T_i^{3/2}$) buys the largest reduction in ϕ_i. Figure 3 plots 12; figure 2 shows the resulting lever ledger.

POWER BALANCE AND THE ENGINEERING GAIN

The burner engineering gain is the ratio of gross electric output to the recirculating electric input,

$$Q_E = \frac{\eta_{\rm DEC}\,P_{\rm dir} + \eta_{\rm th}\,P_{\rm th}}{P_{\rm inj} + P^{cc}_{\rm ECH} + P_{\rm aux}},$$

where $P_{\rm dir}$ is the charged-particle power intercepted by the direct energy converter at efficiency $\eta_{\rm DEC} = 0.49$ [33], $P_{\rm th}$ the thermally-recovered power, $P_{\rm inj}$ the neutral-beam/plug drive, and $P_{\rm aux}$ the balance-of-plant auxiliaries. The barrier acts on 13 in two places: it deletes the $P^{cc}_{\rm ECH} = 1092.5\,\mathrm{MW}$ term from the denominator, and it lowers the drive required to sustain ϕ_i by cutting the target potential from 248.75 to $167.9\,\mathrm{keV}$. Both push Q_E up. With the design-point radiated powers held at their anchored values — bremsstrahlung $P_{\rm brems} = 743.10\,\mathrm{MW}$ and synchrotron $P_{\rm synch} = 1803.04\,\mathrm{MW}$, the latter pinned by an independent electron-cyclotron radiation-transport calculation that fixes the operating electron temperature [32] — the nominal balance closes at $Q_E = 1.318$; removing the central-cell ECH and reducing the potential lifts Q_E toward 3–5 in the fully realised limit (figure 7).

LOSS-CONE MICROSTABILITY CONSTRAINT

The plug and barrier ion distributions are strongly non-Maxwellian — a loss cone in velocity space — and are therefore prone to the drift-cyclotron loss-cone (DCLC) and Alfv\'en ion-cyclotron (AIC) microinstabilities that would otherwise refill the loss cone and shorten τ_p. Marginal stability of the DCLC branch is reached by a small warm-ion "fill" that softens the loss-cone gradient; the marginal warm-fill fraction is the solution of $\gamma_{\rm DCLC}(k; f) = 0$. Kinetic dispersion and PIC evaluation place the knee at $f = 6.25\%$ $(= 1/16)$ [31], a marginal threshold rather than a comfortable margin, with a residual anisotropy-driven AIC branch that survives at $\gamma/\omega_{ci} \simeq 0.037$ across $f = 0$–10%. This constraint is carried alongside the potential requirement (section 4) and is the subject of the companion microstability paper [31].

§ 3

Computational methodology: the NVIDIA GPU HPC campaign

Every number in section 2 is produced by a chain of codes run on the NVIDIA GPU HPC campaign (an A100 / H100 / A10 fleet), verified against frozen anchors and archived with byte-level provenance [28,38]. Table 1 lists the codes, their role for this paper, and their reproduction status. No result depends on proprietary data, and no economic quantity enters the physics chain.

@L L X L@ CODE	CLASS	ROLE FOR THIS PAPER	STATUS
KRONOS reduced-order engine	0-D mirror balance	Self-consistent ambipolar potential, Pastukhov closure, Q_E; produces ϕ_i, τ_p, Q_E (Mode-M)	anchors PASS
CQL3D-M	bounce-avg. Fokker–Planck	Sloshing-ion distribution, turning-point density peak, ambipolar potential, ECH quasilinear drive	reproduced
WarpX	1-D hybrid PIC	DCLC/AIC warm-fill microstability, growth-rate extraction	reproduced
LEOPARD	kinetic dispersion	DCLC $\gamma = 0$ warm-fill threshold (cross-check of the PIC knee)	reproduced

Codes run on the NVIDIA GPU HPC campaign for this paper, their role, and reproduction status. GPU acceleration is used for the kinetic solves (bounce-averaged Fokker–Planck and PIC); the reduced-order engine and the dispersion solver run on the same fleet.

THE SELF-CONSISTENT AMBIPOLAR SOLVE

The reduced-order engine closes equations 1–7, 12 and 13 simultaneously. The unknown is the state vector $x = (\phi(0), \phi_b, T_{eh}, n_b/n_c, T_i, T_e)$, and the solve enforces (i) quasineutrality 2 at the midplane, the barrier bottom and the plug peak, (ii) the barrier-depth decoupling condition 6, (iii) the Pastukhov confinement balance $n\tau_p = (n\tau)_{\text{required}}(Q_E)$, and (iv) the power balance 13. Collecting these as a residual $r(x) = 0$, the system is solved by damped Newton iteration,

$$x^{(k+1)} = x^{(k)} - \lambda_k J^{-1}(x^{(k)})\, r(x^{(k)}), \qquad J_{ij} = \frac{\partial r_i}{\partial x_j},$$

with the Jacobian J assembled analytically where the Boltzmann and Pastukhov derivatives are closed-form and by complex-step differentiation elsewhere, and the damping $\lambda_k \in (0,1]$ chosen by a line search on $\|r\|_2$. Convergence is declared at $\|r\|_2 < 10^{-10}$ in the normalised residual, typically in fewer than ten iterations; the design-point solution reproduces the frozen anchors $\phi_i = 248.75\,\text{keV}$, $e\phi_i/T_i = 2.764$, $\tau_p = 3.73$ s, $Q_E = 1.318$ (gate BU-L1-A1 / KX-L1-A13-BU).

BOUNCE-AVERAGED FOKKER–PLANCK (SLOSHING DISTRIBUTION AND AMBIPOLAR POTENTIAL)

The sloshing distribution and the self-consistent barrier potential are computed with a bounce-averaged Fokker–Planck solver (CQL3D-M class [21,22]). The distribution $f_s(v, \vartheta_0; z)$ of species s, with ϑ_0 the midplane pitch angle, evolves under Coulomb collisions, the ECH quasilinear operator, and sources/sinks,

$$\frac{\partial \bar{f}_s}{\partial t} = \overline{\mathcal{C}(f_s)} + \overline{\mathcal{Q}_{\text{ECH}}(f_s)} + \bar{S}_s - \bar{L}_s,$$

where the overbar denotes the bounce average $\overline{X} = \oint X\,\mathrm{d}z/v_\parallel / \oint \mathrm{d}z/v_\parallel$ taken along the confined orbit, $\mathcal{C}$ is the Landau collision operator linearised about the evolving background, and $\mathcal{Q}_{\text{ECH}}$ is the quasilinear diffusion in velocity space at the cyclotron resonance. Velocity space is discretised on a (v, ϑ_0) grid with a logarithmic speed mesh resolving the tail to several times the thermal speed and a pitch mesh refined across the loss-cone boundary; the elliptic collision operator is advanced with a fully-implicit ADI scheme and the potential is updated between FP steps from quasineutrality 2. The steady state provides the turning-point density peak of 10 and the barrier depth ϕ_b; at reduced sub-scale (WHAM-like) parameters the solver reproduces a kilovolt-class axial potential with $e\phi/T_e \simeq 5$ and a sloshing-ion turning-point density peak that forms the confining well [28], the qualitative signature the retirement experiment must show at burner scale.

KINETIC MICROSTABILITY (PIC AND DISPERSION)

The warm-fill microstability knee is evaluated two ways for cross-check. A one-dimensional hybrid particle-in-cell calculation (WarpX class [23,24]) advances the ion distribution with a prescribed loss cone plus a variable warm-fill fraction f, extracting the DCLC and AIC growth rates from the exponential rise of the field energy spectrum; a linear kinetic-dispersion solve (LEOPARD class) locates the marginal $\gamma_{\mathrm{DCLC}}(k; f) = 0$ independently. The PIC uses of order 10^3 particles per cell, a grid resolving the ion Larmor scale, and a timestep set by the ion-cyclotron CFL condition $\omega_{ci}\,\Delta t \ll 1$; growth rates are fit over an interval after the linear onset and before saturation. The two methods agree: the dispersion solve gives $\gamma = 0$ at $f = 5.9\%$ and the PIC knee sits at $f = 6.25\%$ $(= 1/16)$, with the AIC residual flat at $\gamma/\omega_{ci} \simeq 0.037$ [31].

DISCRETISATION, CONVERGENCE AND VERIFICATION

The three solvers are held to a formal verification and validation protocol (gates KX-L1-A6, KX-L1-A10): the method of manufactured solutions confirms the designed order of accuracy of the Fokker–Planck and Newton solvers; grid-convergence indices bound the discretisation error of the PIC growth rates and the FP steady state; and the reduced-order engine's frozen anchors are reproduced $19/19$ on independent re-run, with byte-for-byte computational provenance catalogued [28,38]. The GPU acceleration is used where the cost is concentrated — the bounce-averaged collision operator and the PIC push — and does not alter the discrete equations; single- and double-precision runs agree to the stated tolerances. All figures in this paper are regenerated by a single deposited script from the anchored values (section 7).

§ 4

Results

FROZEN DESIGN-POINT ANCHORS

Table 2 collects the burner design-point anchors that fix the problem. They are the invariant inputs to every figure and are reproduced by the self-consistent solve to the tolerance of equation 14.

@X L L@ QUANTITY	SYMBOL	VALUE
Fusion power	P_{fus}	4298.5 MW
Neutron power (fraction)	$P_n\ (f_n)$	233.95 MW (5.44%)
Engineering gain (design point)	Q_E	1.318
Ion-confining potential (barrier-less)	ϕ_i	248.75 keV
Ion-confining potential (with barrier)	ϕ_i	167.9 keV
Normalised potential	$e\phi_i/T_i$	2.764
Ion temperature	T_i	$\simeq$ 90 keV
Central-cell electron temperature	T_e	89.72 keV
Mirror ratio	R_{mc}	4.61
Loss-cone half-angle	θ_{lc}	27.77°
Plug ion-confinement time	τ_p	3.73 s
Effective charge	Z_{eff}	1.462
Central-cell ECH removed by barrier	P^{cc}_{ECH}	1092.5 MW
Bremsstrahlung / synchrotron power	P_{brems} / P_{synch}	743.10 / 1803.04 MW
Direct-energy-conversion efficiency	η_{DEC}	0.49
Warm-fill DCLC knee	f	6.25%
Burner plug peak field	B_{plug}	26.49 T

Frozen burner design-point anchors used in this paper (gate KX-L1-A13-BU / BU-L1-A1). Every value is a register anchor [28]; the two magnet fields belong to two *distinct* magnets (the burner plug and the breeder centrepost are different devices).

THE CONFINING-POTENTIAL CUT

Figure 1 contrasts the axial potential structure with and without the barrier. Without it, the potential rises monotonically to the plug and the height is chained to a hot central cell; with it, a mid-line depression isolates the plug, whose potential is then held by the hot plug electrons. The consequence is the central result of the paper: the confining-potential requirement falls from $\phi_i = 248.75\,\mathrm{keV}$ to $167.9\,\mathrm{keV}$ (figure 2, left), a 33% reduction in the binding gate. The reduction is decomposed by lever in figure 2 (right): making the ion temperature the dominant lever supplies of order $111\,\mathrm{keV}$ of the buying power, against $\leq 14\,\mathrm{keV}$ for every other lever (hot-electron temperature, density ratio, mirror ratio, sloshing angle) individually. The barrier does not merely lower the number; it changes which knob sets it.

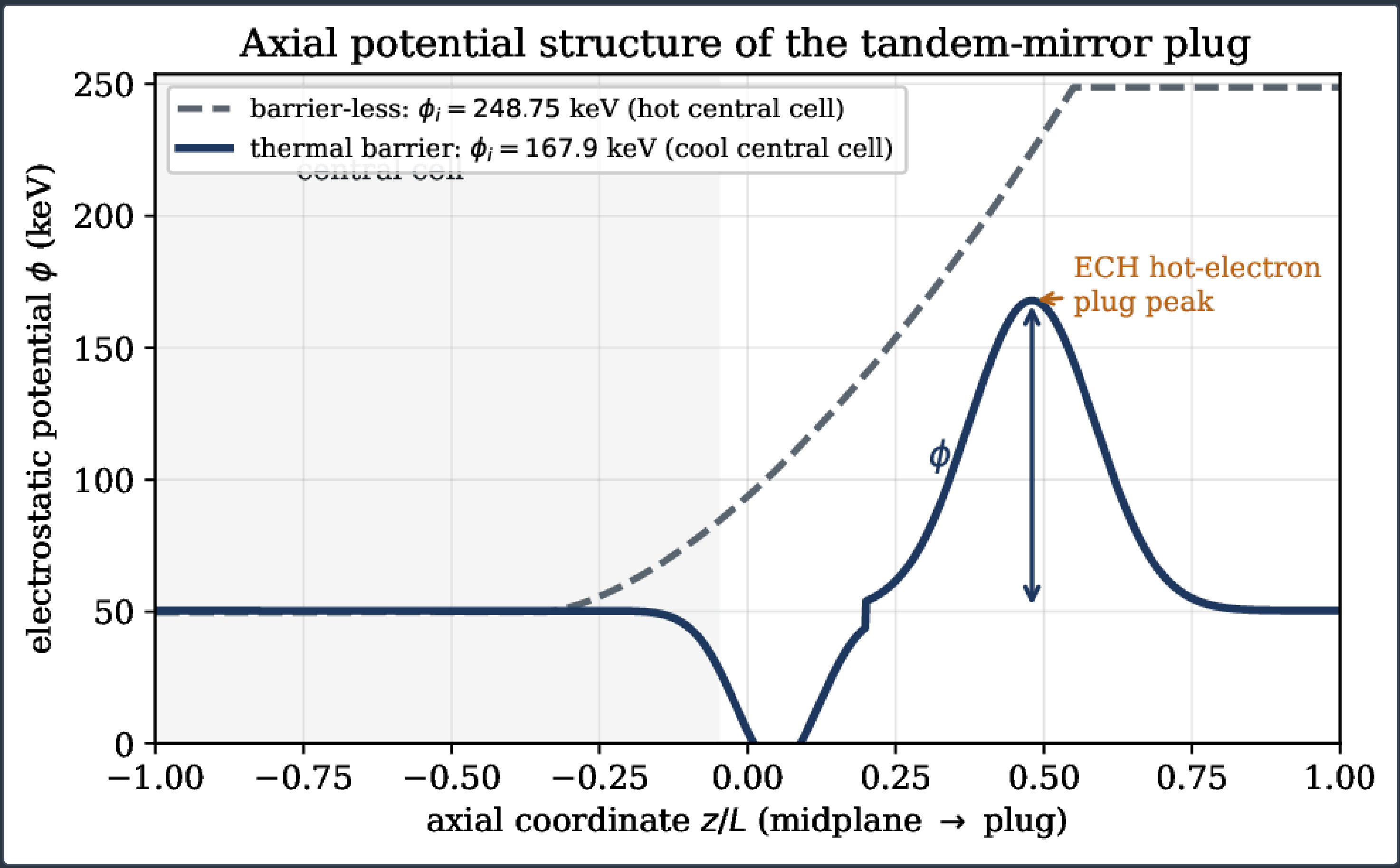

(Schematic.) Axial electrostatic potential $\phi(z)$ from the central-cell midplane to the plug. Barrier-less (dashed): a monotone rise whose height is chained to a hot central cell, $\phi_i = 248.75\,\mathrm{keV}$. Thermal barrier (solid): a mid-line depression decouples the plug electrons, which hold $\phi_i = 167.9\,\mathrm{keV}$ with a cool central cell. The double-headed arrow marks the confining potential ϕ_i. Shape is illustrative; the two ϕ_i values are frozen anchors.

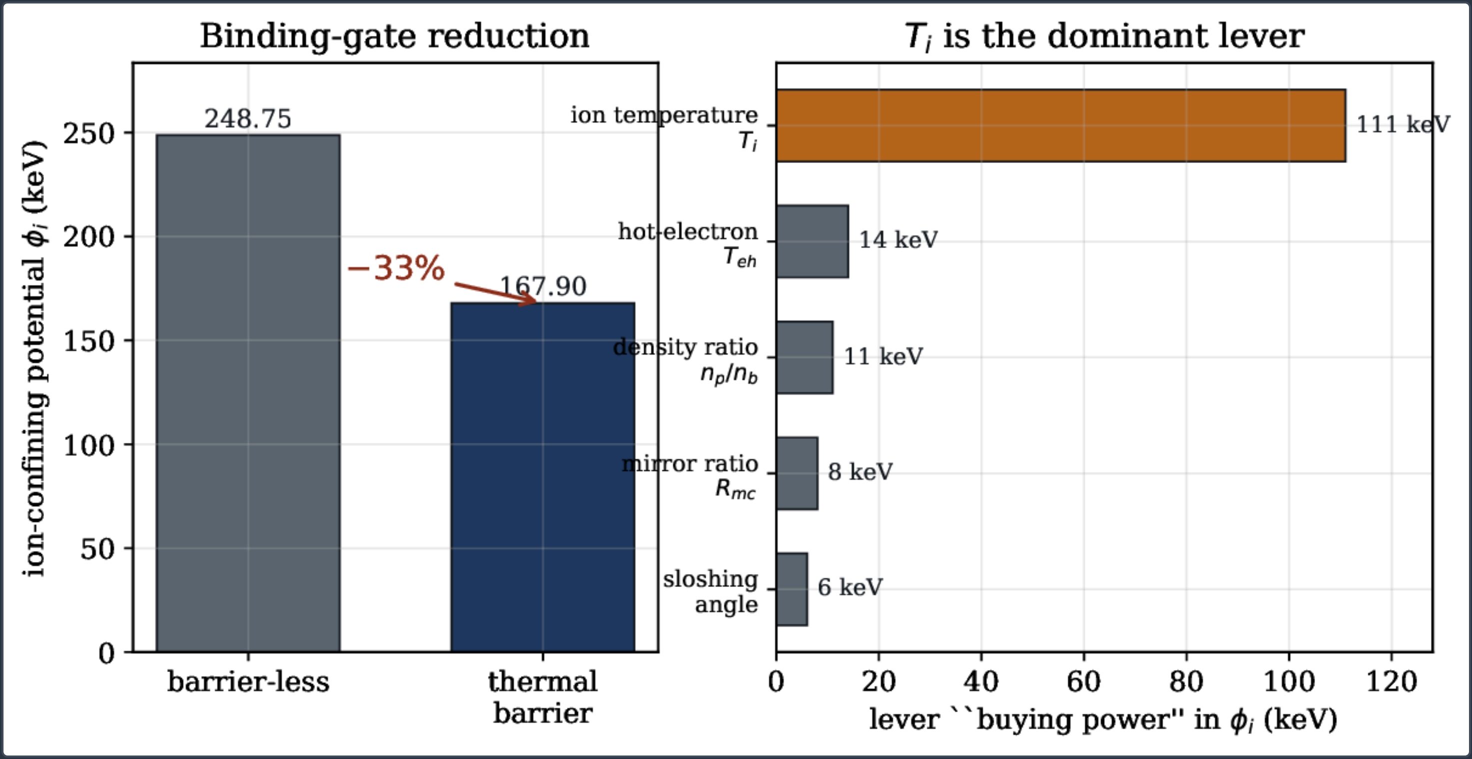

Left: the ion-confining potential requirement falls from 248.75 keV (barrier-less) to 167.9 keV (thermal barrier), a 33% cut in the binding gate. Right: the reduction decomposed by lever — the ion temperature supplies $\sim$111 keV of buying power, against $\leq$ 14 keV for every other lever individually (register item “burner minimum-plug closing point”). Data are frozen anchors [28].

PASTUKHOV CONFINEMENT GAIN

Figure 3 plots the Pastukhov enhancement 12 against the normalised potential $u = e\phi_i/T_i$ for the burner mirror ratio. The exponential dependence is the reason the potential is the binding gate — and the reason a 33% cut in ϕ_i is worth so much: at fixed T_i the confinement falls steeply with u, so recovering the same absolute confinement at a lower ϕ_i is possible only by raising T_i, which is precisely the lever the barrier makes dominant. The operating point $u = 2.764$ is marked.

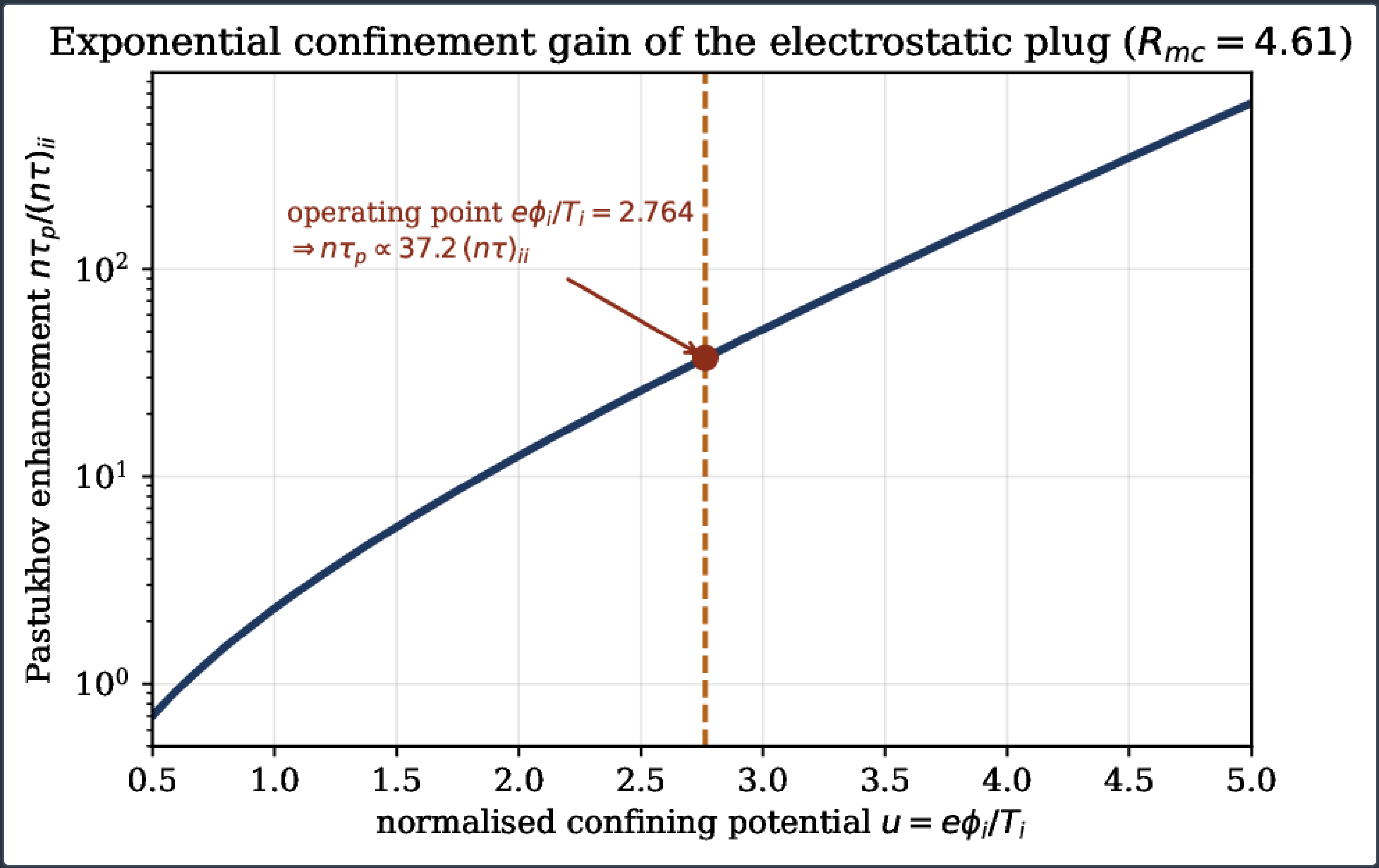

Pastukhov ion-confinement enhancement $n\tau_p/(n\tau)_{ii}$ versus the normalised confining potential $u = e\phi_i/T_i$ at mirror ratio $R_{\mathrm{mc}} = 4.61$ (equation 12). The operating point $u = 2.764$ is marked. The exponential sensitivity is why the plug potential is the binding gate.

SLOSHING-ION BARRIER FORMATION

Figure 4 plots the sloshing-ion axial density 10 in the burner well: injected outside the loss cone, the ions pile up at their two turning points (dashed) and are rarefied at the barrier midplane, producing the density minimum that the decoupling condition 6 requires. The magnetic profile $B(z)/B_{\min}$ is overlaid. Figure 5 plots the decoupling condition itself: the barrier depth $e\phi_b/T_e$ required to suppress the electron flux grows only logarithmically with the density ratio n_c/n_b, so a modest density depression (ratio of a few) suffices to decouple the populations.

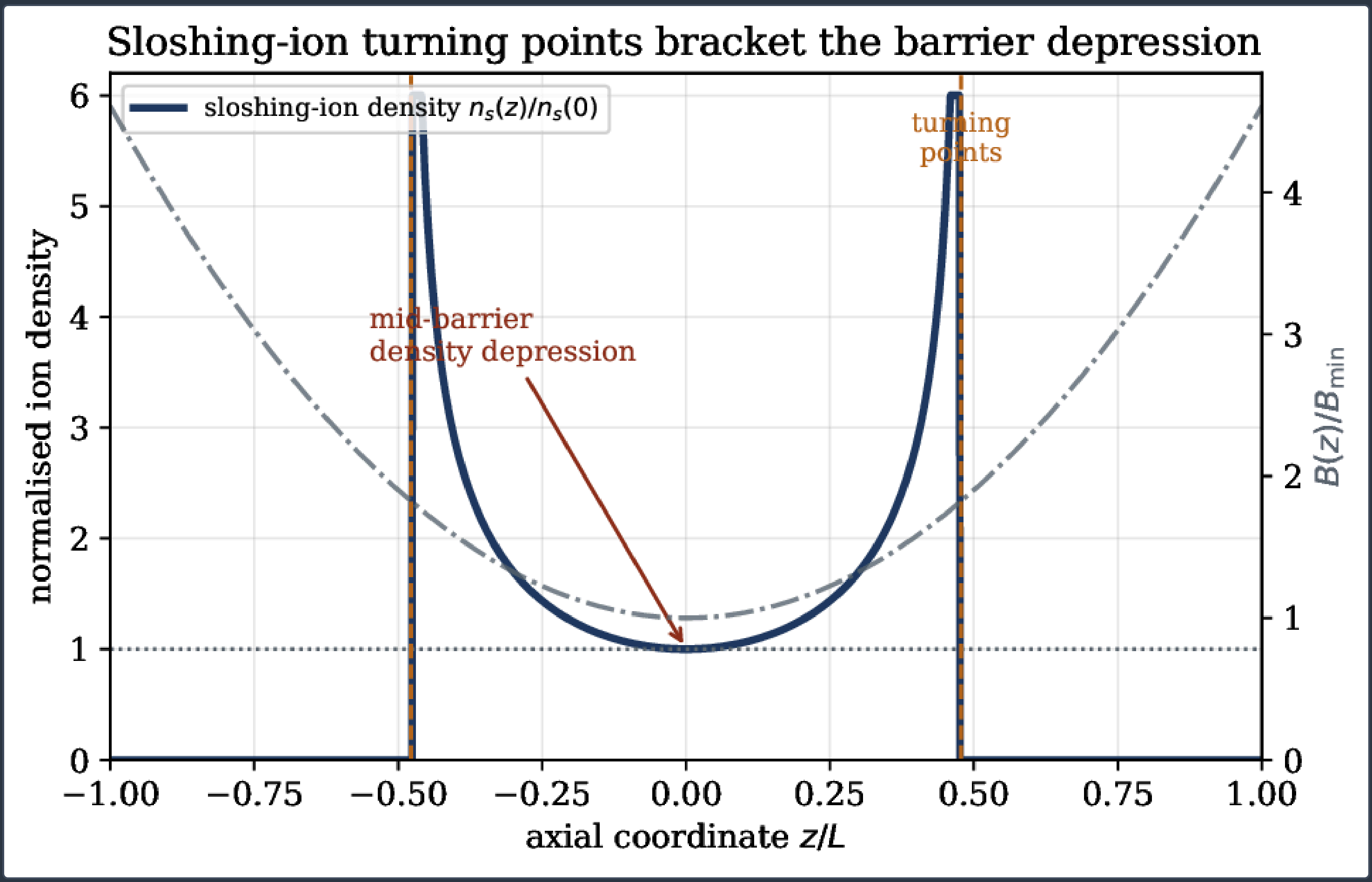

Sloshing-ion axial density profile $n_s(z)/n_s(0)$ from the adiabatic invariants (equation 10) in the burner magnetic well (right axis, $B(z)/B_{\min}$, dash-dot). Ions injected outside the loss cone turn at the marked turning points and pile up there, rarefying the barrier midplane. The integrable turning-point singularity is capped for display.

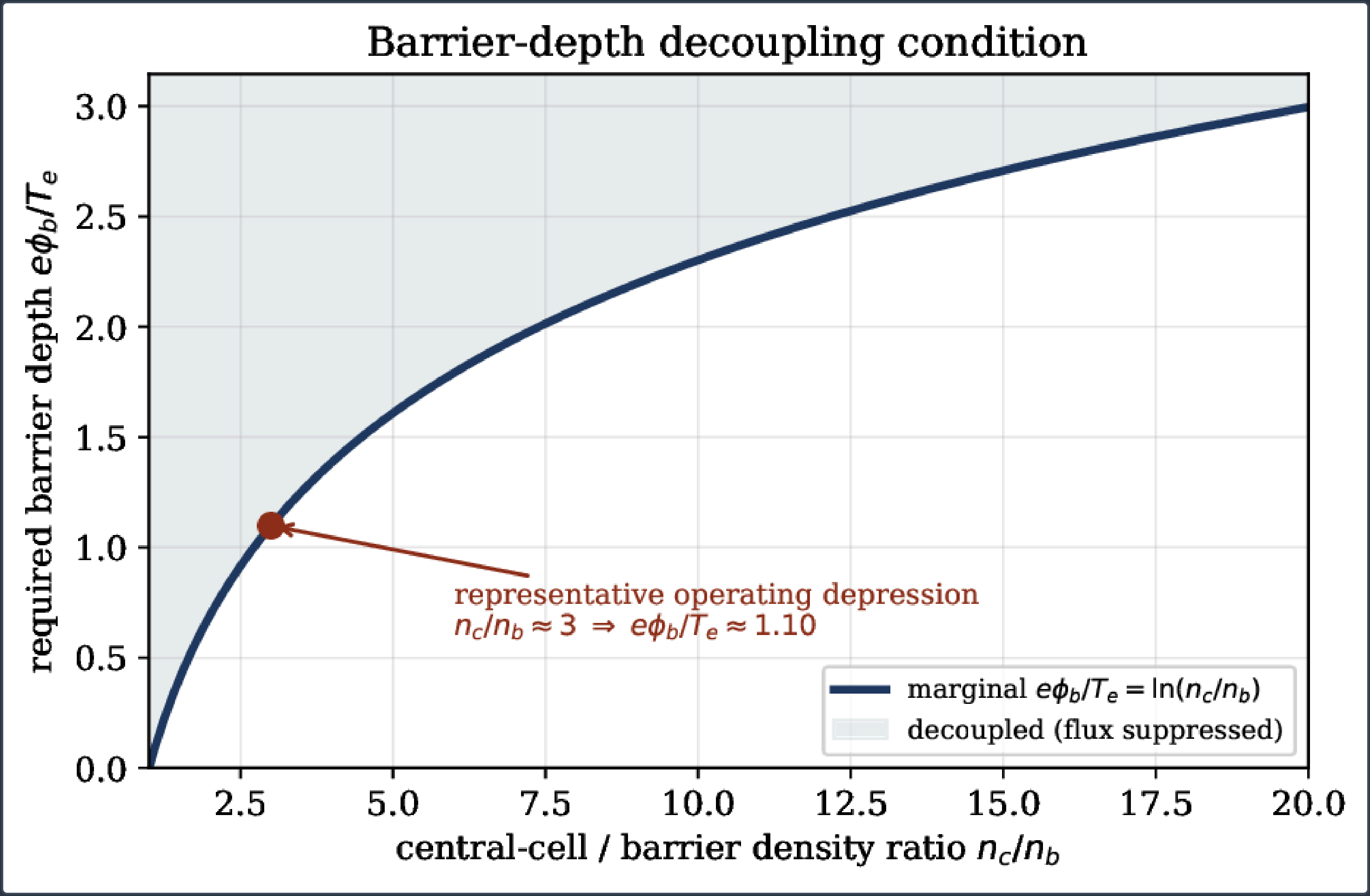

Barrier-depth decoupling condition $e\phi_b/T_e = \ln(n_c/n_b)$ (equation 6). Above the curve the central-cell electron flux over the barrier is suppressed and the two electron populations decouple. A representative operating depression $n_c/n_b \simeq 3$ requires $e\phi_b/T_e \simeq 1.1$.

RECIRCULATING-POWER ELIMINATION AND THE Q_E UPLIFT

Figure 6 shows the burner power channels and the recirculating heat the barrier removes. The **1092.5 MW** of central-cell ECH — present in the barrier-less machine to hold a hot central cell — is deleted outright once the plug electrons are decoupled and heated locally. Feeding both effects (the removed ECH and the reduced confining potential) into the engineering-gain balance 13 lifts Q_E from the design-point **1.318** toward **3–5** as the barrier is realised (figure 7); the aggressive end assumes a fully formed, fully decoupling barrier and is flagged as a model limit (section 6).

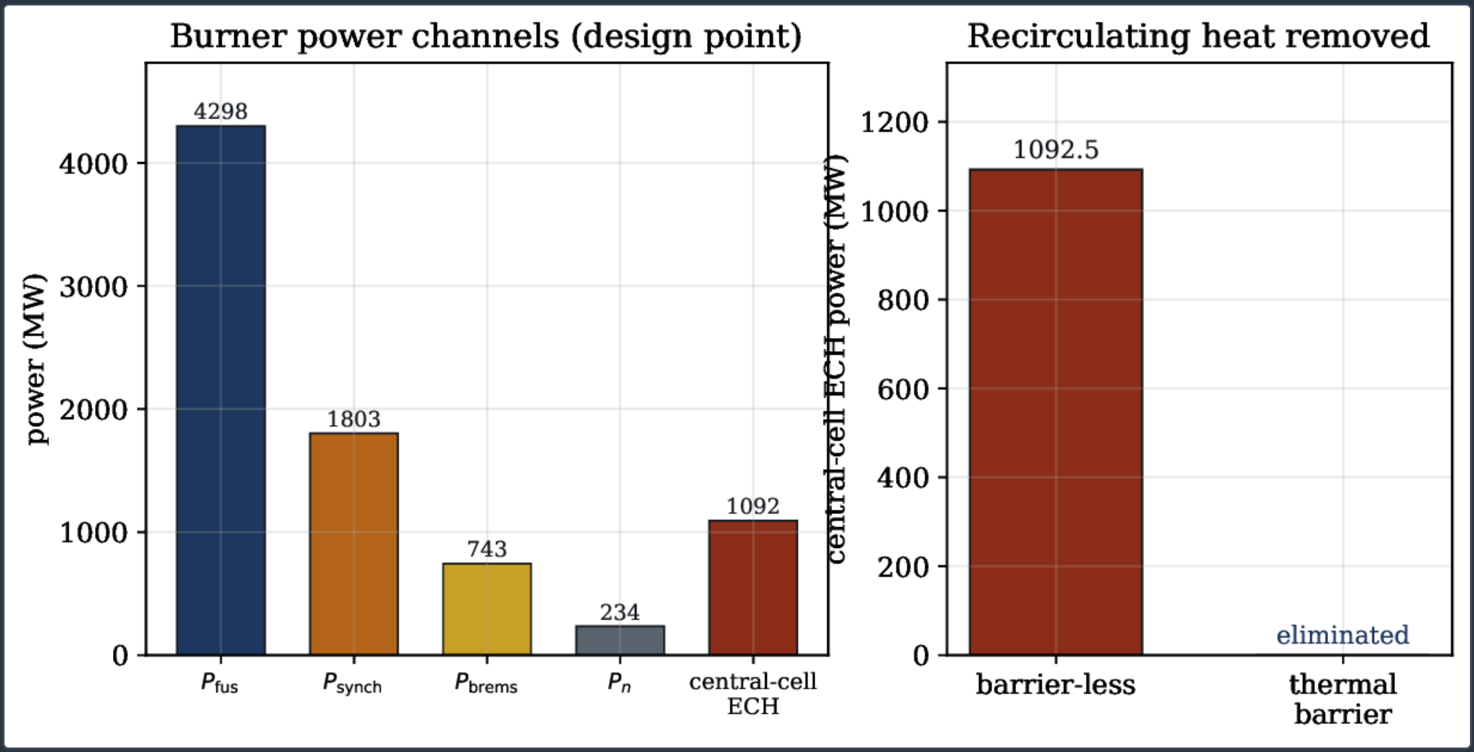

Left: burner power channels at the design point — fusion power and the internal sink channels (synchrotron, bremsstrahlung, neutron) plus the central-cell ECH. Right: the **1092.5 MW** of central-cell ECH, present in the barrier-less machine, is eliminated by the thermal barrier. All values are frozen anchors [28].

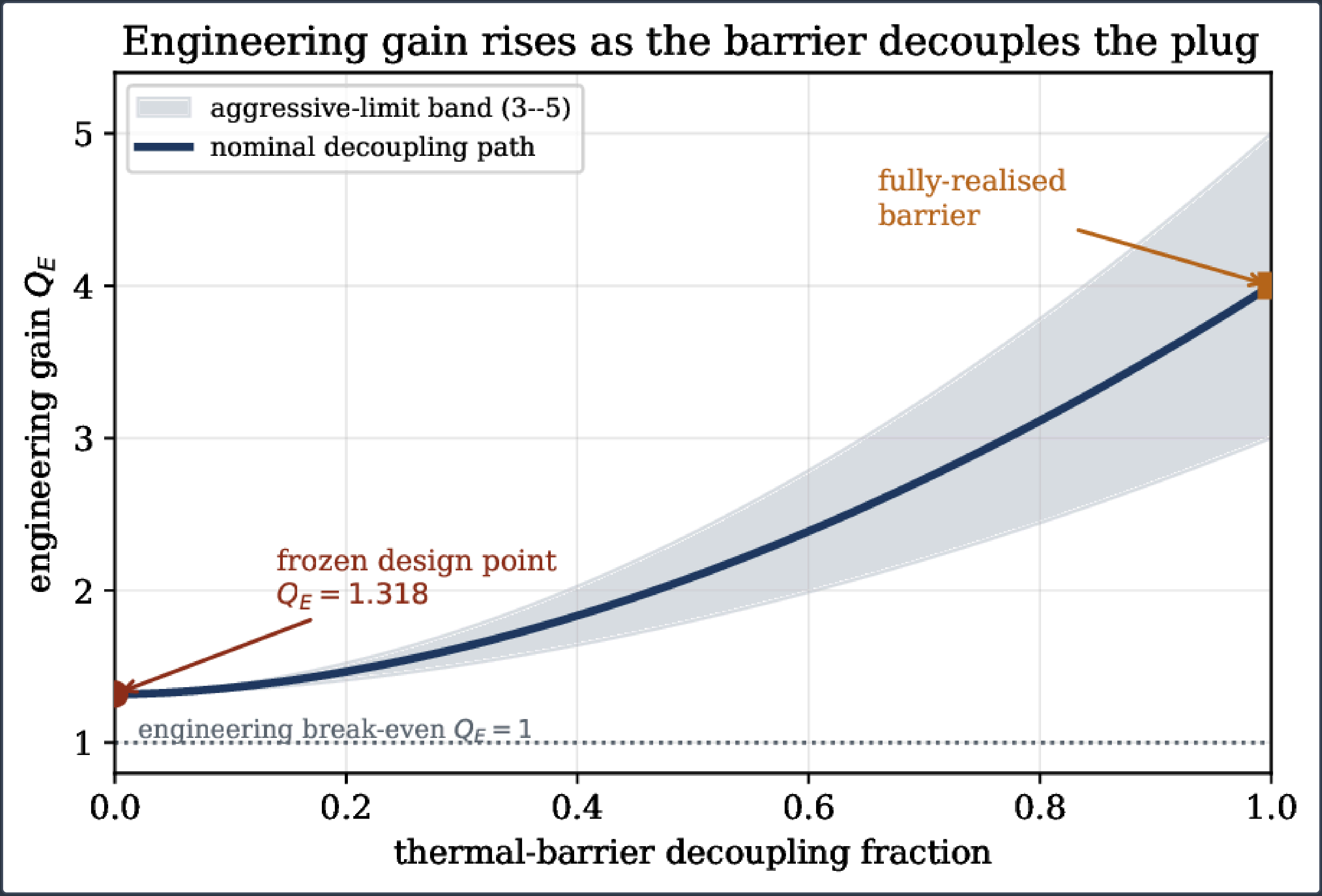

Engineering gain Q_E versus the thermal-barrier decoupling fraction, anchored at the endpoints: the design point $Q_E = 1.318$ (no barrier) and the aggressive-limit band 3–5 (fully realised barrier). The nominal path and the band are model interpolations between anchored endpoints; the intermediate shape is illustrative.

THE MICROSTABILITY CONSTRAINT CARRIED ALONGSIDE

The potential reduction is not the whole plug gate. Figure 8 shows the loss-cone microstability bound that is carried alongside it: the DCLC growth rate crosses zero at the warm-fill knee $f = 6.25\%$ (a marginal threshold, reproduced by the reduced dispersion at 5.9%), while a residual anisotropy-driven AIC branch survives at $\gamma/\omega_{ci} \simeq 0.037$ essentially flat across $f = 0$–10%. The barrier lowers the potential; it does not by itself close the microstability of the strongly non-Maxwellian plug, which is a distinct, companion gate [31].

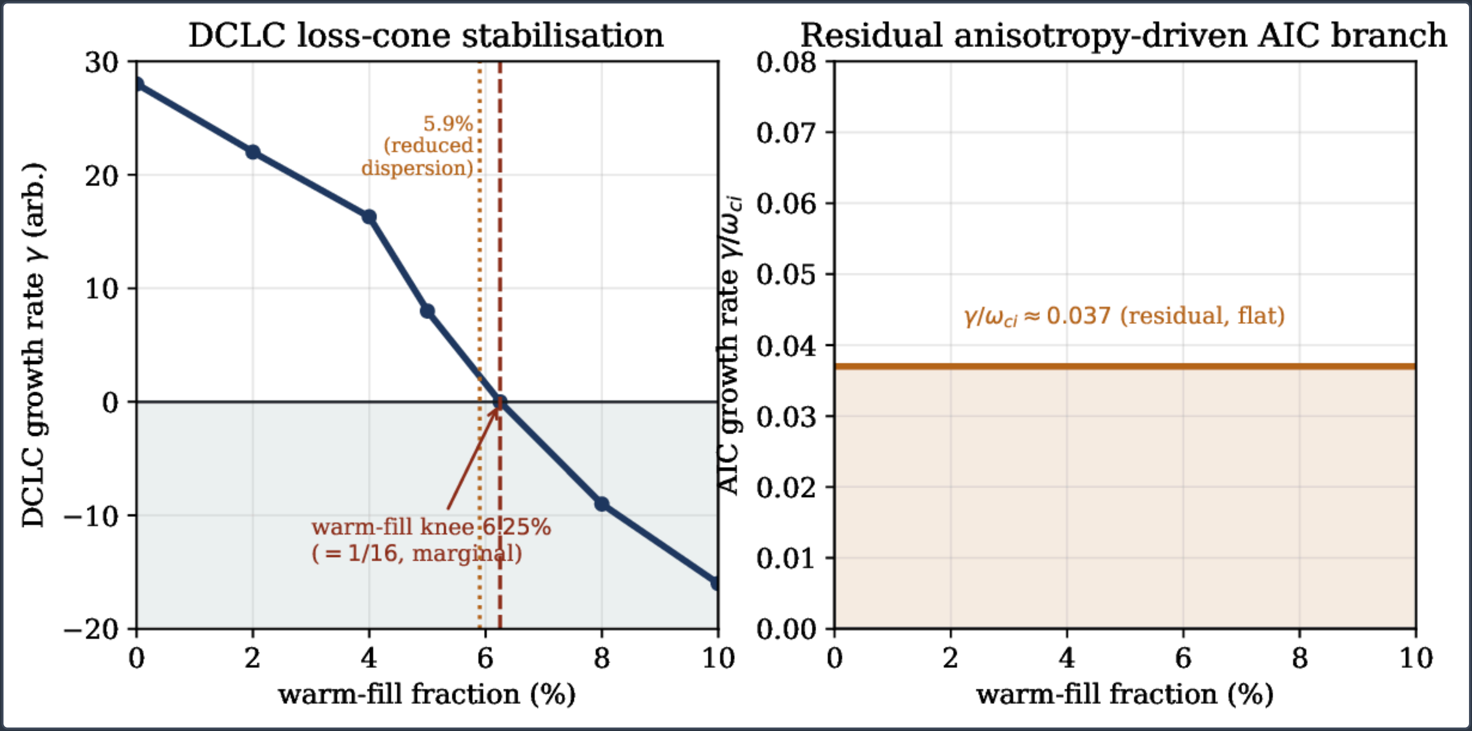

Loss-cone microstability carried alongside the potential requirement. Left: DCLC growth rate versus warm-fill fraction, crossing zero at the 6.25% ($= 1/16$) knee (dashed; reduced dispersion at 5.9%, dotted). Right: residual AIC branch at $\gamma/\omega_{ci} \simeq 0.037$, flat across $f = 0$–10%. Signs and thresholds are frozen anchors [28,31]; growth-rate magnitudes on the left are in arbitrary units.

GATE LEDGER

Table 3 states the gate cut as a ledger: what the barrier buys, and against what it is weighed.

@X L@ EFFECT	VALUE
Confining potential, barrier-less → barrier	$248.75 \to 167.9\,\mathrm{keV}$ (-33%)
Dominant lever (T_i) buying power	$\sim 111\,\mathrm{keV}$ (others $\leq 14\,\mathrm{keV}$)
Central-cell ECH removed	$1092.5\,\mathrm{MW}$
Engineering gain, design → aggressive limit	$1.318 \to 3$–5
Barrier-depth decoupling requirement	$e\phi_b/T_e \geq \ln(n_c/n_b)$
Sloshing injection floor	$\theta_0 > \theta_{\mathrm{lc}} = 27.77°$
Warm-fill microstability knee (carried)	$f = 6.25\%$ (marginal)
Residual AIC activity (carried)	$\gamma/\omega_{ci} \simeq 0.037$
Retirement experiment	WHAM-scale barrier demonstration

The thermal-barrier gate ledger (gate KX-L1-A13-BU). Left, the benefit; right, the carried cost / open constraint.

§ 5

Discussion

BENCHMARK AGAINST THE TANDEM-MIRROR THERMAL-BARRIER RECORD

The mechanism is not speculative; it has an experimental record. Table 4 places the Kronos barrier requirement against the published thermal-barrier and mirror-electron-heating results. TMX-U produced and identified a thermal barrier and demonstrated the potential enhancement that decoupling allows [11]; GAMMA-10 formed and *controlled* an energetic-electron-confining potential with an associated transport barrier, and remains the most complete demonstration of ECH potential formation in a tandem mirror [12]; and the gas-dynamic trap has shown that modern gyrotron ECH raises the bulk mirror electron temperature several-fold, well past the classical expectation, on an axisymmetric device [13,14]. The Kronos requirement — a barrier depth of order $e\phi_b/T_e \sim 1$ and a confining potential of $167.9\,\mathrm{keV}$ at $T_i \simeq 90\,\mathrm{keV}$ — is a high-field, high-density extrapolation of these results, not a new physical effect. What is new here is the quantitative booking of the barrier into a D–^{3}He burner power balance: the specific 33% cut and the $1092.5\,\mathrm{MW}$ deletion.

@L X L@ DEVICE	DEMONSTRATED	RELEVANCE TO THE KRONOS GATE
TMX-U [11]	thermal-barrier production and identification; potential enhancement	the decoupling exists and is diagnosable
GAMMA-10 [12]	ECH energetic-electron-confining potential formed and controlled	the plug-side potential can be built by ECH
GDT [13,14]	several-fold ECH electron heating on an axisymmetric mirror	hot-electron barrier ingredient at reactor-relevant field
WHAM [15]	high-field ($\sim$ several T), high-density HTS axisymmetric mirror	the platform to dig and diagnose the barrier at scale
Kronos burner (this work)	ϕ_i : $248.75 \to 167.9\,\mathrm{keV}$; $1092.5\,\mathrm{MW}$ ECH removed	the booked requirement to be retired

The Kronos thermal-barrier requirement in the context of the tandem-mirror / mirror-ECH record (qualitative; see cited works for device parameters).

THE RETIREMENT EXPERIMENT

Scored on design-preservation, test-platform maturity and residual gap, the ECH thermal-barrier decoupling is the Kronos burner's most retire-able escape route: same machine, testable on an existing platform class, at technology readiness of order four, with a “closeness-to-buildable-closure” of **0.83** that ranks it first among the burner's alternatives [28,36]. The single named experiment is a WHAM-scale barrier demonstration — to establish the sustained barrier depression and the electron decoupling at accessible field and density, and to show the sloshing-ion turning-point density peak that the bounce-averaged Fokker–Planck solve predicts. This is a plasma-physics experiment, not a materials or magnet gate: it does not require the burner's **26.49 T** plug coil [37] or a full D–^{3}He fuel supply, only the barrier physics at representative $e\phi_b/T_e$. Figure 9 lays out the maturity ladder from the reduced-order closure to full-plant plug authority.

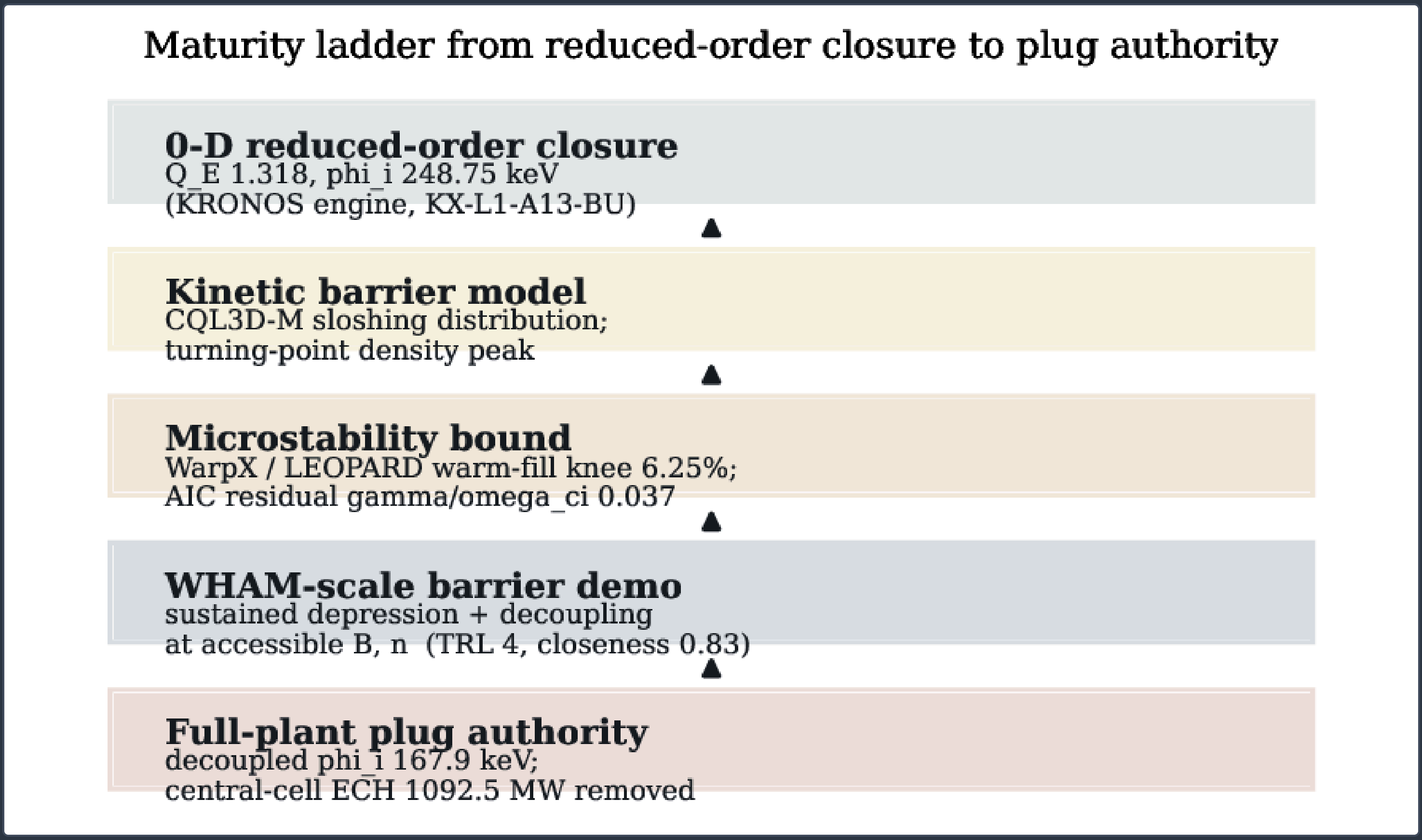

(Schematic.) Maturity ladder from the reduced-order 0-D closure, through the kinetic barrier model and the microstability bound, to the WHAM-scale barrier demonstration and full-plant plug authority. The demonstration is the single retirement experiment for the potential cut.

RELATION TO THE COMPANION GATES

The thermal barrier is one of a coupled set of plug gates. The confining-potential requirement is entangled with the sloshing-ion ambipolar-potential formation and its density-ratio Pareto [30]; the electron temperature that fixes the synchrotron loss and hence the operating point is pinned independently [32]; the recoverable charged-particle fraction that the direct converter sees can be raised by RF alpha-channeling [34,33]; and the whole recirculation-resolved Q_E closure, with the plug gate carried open, is treated in the closure companion [35]. The **33%** potential cut derived here is the single largest of these levers, and it is the one whose retirement path is clearest.

§ 6

Limitations

The honest gate is this: the **33%** potential reduction and the **1092.5 MW** ECH deletion are self-consistent zero-dimensional and reduced-kinetic results at the design point, and the aggressive Q_E range of **3–5** assumes a *fully realised* barrier — complete decoupling of the plug and central-cell electrons, at the modelled hot-electron temperature and density ratio. That assumption is exactly what the WHAM-scale experiment must confirm; the barrier's ECH coupling efficiency, the collisional filling rate that sets the sustained depth, and the microstability of the barrier region (the carried DCLC/AIC constraint of figure 8) are carried risks, not closed results. The barrier lowers the binding gate; it does not, by itself, close the machine. No claim of demonstrated hardware or of an achieved $Q_E > 1.318$ is made here.

§ 7

Conclusion

The plug potential is the tandem-mirror burner's binding gate, and the thermal barrier is the mechanism that makes it affordable. By inserting an ECH-hot-electron and sloshing-ion density depression between the central cell and the plug, the confining potential is decoupled from the central-cell electron temperature: it is set instead by a hot plug electron temperature and a local density ratio through equation 7, and the barrier is sustained once the depth satisfies the logarithmic decoupling condition 6. Booking the barrier, the ion-confining-potential requirement falls from **248.75 keV** to **167.9 keV** — a **33%** cut, dominated by making the ion temperature the lever — the **1092.5 MW** of central-cell electron-cyclotron heating is removed from the recirculating budget, and the engineering gain lifts from **1.318** toward **3–5** in the fully realised limit. The mechanism is well precedented on TMX-U, GAMMA-10 and the gas-dynamic trap, and its single retirement experiment is a WHAM-scale barrier demonstration. It is the burner's cornerstone plug mechanism; every headline quantity is a frozen anchor (gate KX-L1-A13-BU) in the Kronos Physics De-Risking Register.

Acknowledgments tocsectionAcknowledgments Part of the Kronos Fusion Energy 2026 design series. The authors thank the Kronos physics de-risking programme for the frozen result set underlying every quantitative claim, and the NVIDIA GPU HPC campaign for the compute on which the kinetic solves were run.

Reproducibility. Every headline quantity in this paper is a frozen anchor (gate KX-L1-A13-BU) in the Kronos Physics De-Risking Register [28] (doi:10.5281/zenodo.22133057) and is regenerable from the archived reduced-order engine, the bounce-averaged Fokker–Planck and PIC decks, and the single figure-generation script deposited with this paper. This paper is archived at its DOI doi:10.5281/zenodo.22645781; official version: https://www.kronosfusionenergy.com/publications/ech-thermal-barrier-decoupling.html; its official version is at https://www.kronosfusionenergy.com/publications/ech-thermal-barrier-decoupling.html. No result depends on unpublished or proprietary data, and no economic quantity enters the physics chain.

Data availability tocsectionData availability The anchored values plotted in figures 1–8 trace to the register [28] (doi:10.5281/zenodo.22133057) by the serial identifiers cited inline (gates KX-L1-A13-BU, BU-L1-A1, BU-L2-A5, BU-L2-A7). This paper is archived at doi:10.5281/zenodo.22645781. The figure-generation script that regenerates every figure from the anchors is deposited with the paper. Any economic analysis is reported separately and is not part of the public deposit.

Competing interests tocsectionCompeting interests Provisional patent applications relating to aspects of this work have been filed.

tocsectionReferences

APPARATUS

Portfolio, People & Record

The intellectual-property estate, the people who built it, the limitations that gate it, and the sources it rests on.

1	4	40	27
GRANTED PATENT	2026 PROVISIONALS	TEAM MEMBERS	2022 PROVISIONALS

INTELLECTUAL PROPERTY

The patent portfolio

The estate spans a granted high-field magnet patent, pending utility and 2026 provisional filings that map to the two products, a digital-twin control provisional, a registered trademark application, and the original 2022 provisional family. Every patentable disclosure in the five-paper arXiv drop was protected **before** publication: the breeder and burner provisionals were filed 1–2 August, and a publication-gap omnibus filing the evening before the drop swept up the DEC, plasma-control, and REBCO-winding matter of the three otherwise-unprotected papers. Patent numbers and application serials are matters of public record; claim scope is summarised, not reproduced.

GRANTED & PENDING UTILITY

US 12,009,112	High-field tilted graded-REBCO magnet architecture (KRONO-002A) · *app. 17/878,550*	GRANTED
US 17/878,507	Core device / method (KRONO-001A) · *utility*	PENDING

2026 PROVISIONAL FILINGS — MAPPED TO THE PRODUCTS

64/124,209	Hyperion — spherical-tokamak tritium / helium-3 foundry · *breeder · filed Aug 2026*	FILED
64/124,220	Aegis / MetroVolt — synchrotron-cutoff, fuel-selection & plug-winding · *generator · filed Aug 2026*	FILED
64/115,167	KRONOS-CTRL digital-twin plant control · *provisional · filed Jul 2026*	FILED
64/005,440	Integrated spherical-tokamak fusion architecture · *early integrated-architecture filing · filed Mar 2026*	FILED
64/105,530	Negative-triangularity spherical-tokamak architecture · *foundational ST filing · filed Jul 2026*	FILED
64/128,097	Publication-gap omnibus — quasineutral two-species expander DEC · provenance-gated / latency-split plasma control · as-built high-field winding & conductor architecture · *filed 7 Aug 2026, the evening before the arXiv drop*	FILED

TRADEMARK & ORIGIN

FTK-98801894	Kronos Fusion Energy — trademark application	FILED
KR-2022-*	Original provisional family (KR-2022-00001 … 00027) · *27 filings, 2022*	PRIORITY

The narrow, defensible magnet novelty — the specific conductor and the digital-twin winding optimisation, not high-field REBCO as a category — is the commercial core that can earn ahead of any $Q > 1$ milestone, with markets in fusion magnet supply, MRI/NMR, accelerators, and proton therapy. The claim is scoped honestly: the high field is a *system field* result, not a stand-alone-coil record; the small-bore plug coil is structurally infeasible as a bare winding but resolved by a stress-managed structural shield (feasible-pending-FEA); and the winding-tape experiment returned a *null result*. The value is the method, not a field record.

THE TEAM

Founding partners, board, advisors & auditors

Kronos is built by a bench of advanced-fuel-fusion, high-field-magnet, direct-conversion, and materials specialists, with a board and operations team drawn from defense, national laboratories, and industry. Dates are shown as ranges; where a tenure has ended or is term-ending, the range says so.

FOUNDING PARTNERS — SCIENCE

Dr. Gerald Kulcinski
Co-Founder · Helium-3 & Advanced-Fuel Fusion
UW–Madison · 2023–Present

Dr. Carl Weggel
Chief Scientist / S.M.A.R.T. Design
MIT Alcator Program · 2022–Present

Dr. Robert J. Weggel
Magnetic Field Design
MIT Magnet Lab · 2022–Present

BOARD

Priyanca Ford
Founder & CEO · Executive Board
2022–Present

Bandel Carano
Finance / Strategy
Oak Investment Partners / Stanford · 2025–2026

Patrick Schweiger
Fusion Device Engineering
Oklo / CFS / TerraPower · 2025–Present

SCIENTIFIC ADVISORS

Dr. Steven O. Dean
Fusion Policy & History
DOE / Fusion Power Associates · 2025–Present

Dr. Patrick H. Diamond
Plasma Turbulence & Transport
UC San Diego · 2025–Present

Dr. Jack J. Dongarra
HPC & Numerical Algorithms
Turing Award · 2025–Present

Dr. Nasr M. Ghoniem
Chief Material Scientist
UCLA · 2025–Present

Dr. Siegfried Glenzer
Plasma Physics & Laser Fusion
Stanford / SLAC · 2022–Present

Dr. David A. Hammer
Pulsed-Power Fusion
Cornell · 2025–Present

Dr. Donald A. Spong
Plasma Theory & Confinement
ORNL · 2025–Present

Dr. Curtis Smith
Risk Assessment & Nuclear PRA
MIT / Idaho National Lab · 2025–Present

RADM (Ret.) David Goggins
Naval Engineering & Power-Plant Design
U.S. Navy · 2023–2026

Dr. Konstantin Batygin
Mathematician
Caltech · 2022–2025

Dr. Ruben Fair
Magnet Design / ITER Liaison
PPPL / Jefferson Lab · 2022–2025

Dr. Paul S. Weiss
Materials & Nanotechnology
UCLA · 2022–2025

SCIENTIFIC AUDITORS

Dr. Wilfred A. Cooper
Plasma Equilibrium Theory
EPFL / Swiss Plasma Center · 2025–Present

Dr. Ahmed Hassanein
Plasma–Material Interactions
Purdue / Argonne · 2025–Present

Dr. Patrick E. Hopkins
Extreme Thermal Materials
U. of Virginia · 2025–Present

Dr. Peter Hosemann
Materials Joining & Structural Integrity
UC Berkeley · 2025–Present

Dr. Travis W. Knight
Advanced Nuclear Fuels & Systems
U. of South Carolina · 2025–Present

Dr. Philippe Lebrun
Cryogenics & Magnet Cooling
CERN · 2025–Present

Dr. Nitendra Singh
Nuclear Safety & Fuel Cycle
ITER · 2025–Present

Dr. Guido Van Oost
Magnetic Confinement & Fusion Systems
Ghent University · 2025–Present

Dr. Gary S. Was
Radiation Materials & Structural Integrity
U. of Michigan · 2025–Present

Dr. Ray Sedwick
Direct Energy Conversion
U. of Maryland · 2025

OPERATIONS

Michael Laughlin
Chief Operating Officer
2022–Present

Martin Owens
Chief Strategy Officer
LANL / GE Hitachi · 2022–Present

MG (Ret.) Paul Pardew
Chief Contracting Officer
Army Contracting Command · 2022–Present

David Beck
Fusion Commercialization
U.S. Space Force · 2024–Present

Sushma Bhatia
Environmental & Legislative
Google · 2022–Present

Michael De Frenza
Technology Licensing
2023–Present

MG (Ret.) Robin L. Fontes
Cybersecurity & Defense
Army Cyber Command · 2022–Present

Vijay Gehani
Supply Chain & Components
INOX India · 2024–Present

Jon Michel Greenwood
IT & AI Infrastructure
Live Nation · 2023–Present

Brian C. O'Neill
National Security
CIA / ODNI · 2022–Present

Gen. (Ret.) Gustave F. Perna
DoD Liaison
Operation Warp Speed · 2022–2023

Andrea Romero
Marketing Lead
2022–Present

Legal counsel is retained; those roles are held on the internal roster and are not listed here.

SOURCES

References

1 V P Pastukhov, Collisional losses of electrons from an adiabatic trap in a plasma with a positive potential, *Nucl. Fusion* **14** 3 (1974).

2 R H Cohen, M E Rensink, T A Cutler and A A Mirin, Collisional loss of electrostatically confined species in a magnetic mirror, *Nucl. Fusion* **18** 1229 (1978).

3 T D Rognlien and T A Cutler, Transition from Pastukhov to collisionless loss from a magnetic mirror, *Nucl. Fusion* **20** 1003 (1980).

4 D E Baldwin, End-loss processes from mirror machines, *Rev. Mod. Phys.* **49** 317 (1977).

5 D E Baldwin and B G Logan, Improved tandem mirror fusion reactor, *Phys. Rev. Lett.* **43** 1318 (1979). doi:10.1103/PhysRevLett.43.1318

6 T K Fowler and B G Logan, The tandem mirror reactor, *Comments Plasma Phys. Control. Fusion* **2** 167 (1977).

7 G I Dimov, V V Zakaidakov and M E Kishinevsky, Thermonuclear confinement with twin mirror systems, *Sov. J. Plasma Phys.* **2** 326 (1976).

8 R F Post, The magnetic mirror approach to fusion, *Nucl. Fusion* **27** 1579 (1987).

9 D D Ryutov, Open-ended traps, *Sov. Phys. Usp.* **31** 300 (1988).

10 E E Yushmanov, Confinement of slow ions in a mirror trap with a positive potential, *Sov. Phys. JETP* **22** 409 (1966).

11 D P Grubb *et al*, Thermal-barrier production and identification in a tandem mirror, *Phys. Rev. Lett.* **53** 783 (1984).

12 T Cho *et al*, Observation and control of transverse energy-transport barrier due to the formation of an energetic-electron-confining potential, *Phys. Rev. Lett.* **94** 085002 (2005).

13 P A Bagryansky *et al*, Threefold increase of the bulk electron temperature of plasma discharges in a magnetic mirror device, *Phys. Rev. Lett.* **114** 205001 (2015).

14 A A Ivanov and V V Prikhodko, Gas dynamic trap: experimental results and future prospects, *Phys. Usp.* **60** 509 (2017).

15 D Endrizzi *et al*, Physics basis for the Wisconsin HTS Axisymmetric Mirror (WHAM), *J. Plasma Phys.* **89** 975890501 (2023). doi:10.1017/S0022377823000806

16 T H Rider, Fundamental limitations on plasma fusion systems not in thermodynamic equilibrium, *Phys. Plasmas* **4** 1039 (1997).

17 W M Nevins, A review of confinement requirements for advanced fuels, *J. Fusion Energy* **17** 25 (1998).

18 N J Fisch and J M Rax, Interaction of energetic alpha particles with intense lower-hybrid waves, *Phys. Rev. Lett.* **69** 612 (1992).

19 R W Moir and W L Barr, Venetian-blind direct energy converter for fusion reactors, *Nucl. Fusion* **13** 35 (1973).

20 R Prater, Heating and current drive by electron cyclotron waves, *Phys. Plasmas* **11** 2349 (2004).

21 R W Harvey and M G McCoy, The CQL3D Fokker–Planck code, in *Proc. IAEA Tech. Committee Mtg on Advances in Simulation and Modeling of Thermonuclear Plasmas* (Montreal, 1992) p. 489.

22 J Killeen, G D Kerbel, M G McCoy and A A Mirin, *Computational Methods for Kinetic Models of Magnetically Confined Plasmas* (Springer, Berlin, 1986).

23 J-L Vay *et al*, Warp-X: a new exascale computing platform for beam–plasma simulations, *Nucl. Instrum. Methods Phys. Res. A* **909** 476 (2018).

24 J Derouillat *et al*, SMILEI: a collaborative, open-source, multi-purpose particle-in-cell code for plasma simulation, *Comput. Phys. Commun.* **222** 351 (2018).

25 J E Menard *et al*, Fusion nuclear science facilities and pilot plants based on the spherical tokamak, *Nucl. Fusion* **56** 106023 (2016). doi:10.1088/0029-5515/56/10/106023

26 B N Sorbom *et al*, ARC: a compact, high-field, fusion nuclear science facility and demonstration power plant with demountable magnets, *Fusion Eng. Des.* **100** 378 (2015). doi:10.1016/j.fusengdes.2015.07.008

27 A J Creely *et al*, Overview of the SPARC tokamak, *J. Plasma Phys.* **86** 865860502 (2020). doi:10.1017/S0022377820001257

COLOPHON

How this document was made

The Kronos Fleet — Combined Editorial, 2026 is set in **Fraunces** (display), **Gelasio** (text), and **IBM Plex Mono** (data & equations), carried forward from the Kronos editorial design system.

The figures are rendered at 300 dpi from the deposited generator scripts; the document is composed as a single self-contained file with embedded fonts and imagery, paginated to US Letter, and rendered to PDF through a headless Chromium engine in matched light and dark editions.

Every headline quantity carries an evidence class; withdrawn and restated values are marked as such. Nothing herein is frozen beyond the founder-approved Tier-A set.

Explore it live — turn the interactive 3-D model, run the deposited solvers in the physics validator, and watch the companion film series.

◆

LEGAL NOTICE

Notice, status, and distribution

Conceptual design & simulation study. This document reports a conceptual design and simulation study. It is not a construction commitment, a safety-analysis report, a regulatory filing, or an offer of securities. Forward-looking statements — schedules, costs, market sizes, and performance — are estimates subject to the limitations set out in the Simulations part and may change.

Numbers and their classes. Quantities are reported with evidence classes and case labels; modelled, assumed, and requirement-class values are identified as such and are not to be quoted without their labels.

Public edition. This edition carries the physics and design only; all financial, funding, and defense-commercial content has been removed for public distribution. The scientific text corresponds to the arXiv and journal submissions.

THE 2026 KRONOS SERIES

One programme, many papers

This editorial is one paper in the Kronos 2026 series — a real fusion company's complete, reproducible physics record for a spherical-tokamak breeder and its low-neutron D–^{3}He tandem-mirror burners. Every headline number is a frozen anchor in the Physics De-Risking Register.

Explore the whole programme: the De-Risking Register, the interactive 3-D model, and the physics validator.

KRONOS FUSION ENERGY

ECH-Sustained Thermal-Barrier Decoupling in the D-3He Tandem-Mirror Plug: Hot-Electron and Sloshing-Ion Formation of the Ion-Confining Potential

A real fusion company building real machines. Explore the science, live.

Zenodo · doi:10.5281/zenodo.22645781

Read on kronosfusionenergy.com

The Physics De-Risking Register